

Facile one-pot synthesis of ultrathin NiS nanosheets anchored on graphene and the improved electrochemical Li-storage properties†

Qin Pan, Jian Xie,* Shuangyu Liu, Gaoshao Cao, Tiejun Zhu and Xinbing Zhao*

Cite this: *RSC Advances*, 2013, 3, 3899

Received 5th October 2012,
Accepted 4th December 2012

DOI: 10.1039/c2ra22410k

www.rsc.org/advances

1. Introduction

Metal sulfides such as FeS_2 ,^{1–3} CoS_x ,^{4–6} MoS_2 ,^{7,8} and NiS ^{9–11} with potential applications as anodes for Li-ion batteries or cathodes for Li batteries have been the subject of considerable interest because of their high theoretical capacity. Among various metal sulfides, nickel sulfide has received a special interest for its high theoretical capacity of 590 mAh g^{-1} .⁹ It is also more favorable in terms of abundant resource, less toxicity and good electronic conductivity.¹² Unfortunately, nickel sulfide shows rapid capacity fade due to the large volume changes during the conversion reactions.^{12,13} Various strategies have been proposed to improve its electrochemical properties, either by particle size minimizing through ball-milling^{9,14} or liquid-phase synthesis techniques,¹⁵ or by morphology modifications.^{11,16} For example, hollow structured NiS/Ni can yield a specific capacity as high as 400 mAh g^{-1} at 5 C and a stable cycling of 100 times at 0.15 C.¹⁶

Forming hybrids with a matrix is another effective measure to improve the electrochemical properties of metal chalcogenides. Promising electrochemical properties of Co_9S_8 could be achieved by fabricating a composite with carbon.¹⁷ The

$\text{NiS}/\text{graphene}$ (NiS/G) nanohybrid has been synthesized by a facile *in situ* one-pot hydrothermal route using graphite oxide, thiourea, $\text{NiCl}_2 \cdot 4\text{H}_2\text{O}$ and sodium citrate as the raw materials. The growth of NiS nanosheets and the reduction of graphite oxide occur simultaneously during the hydrothermal reactions. The hybrid exhibits a unique sheet-on-sheet structure, where ultrathin NiS sheets (below 5 nm) are anchoring on few-layer (below 8 layers) graphene sheets. The electrochemical measurements indicate that the NiS/G hybrid exhibits remarkably improved Li-storage properties compared with bare NiS , due to the ultrathin feature of the NiS sheets, unique sheet-on-sheet structure of the hybrid, and the combined conducting, buffering and confining effects of the *in situ* introduced graphene nanosheets.

electrochemical performance of SnO_2 can also be improved obviously by forming a hybrid with carbon.¹⁸ The hybrid structure was also used to improve the electrochemical performance of Si anodes.^{19,20} Recently, graphene-based hybrids such as $\text{NiO}/\text{graphene}$,^{21–23} $\text{MoS}_2/\text{graphene}$,^{24,25} and $\text{CoS}_2/\text{graphene}$ ²⁶ have been reported to exhibit extraordinarily high electrochemical performance, indicating that graphene, a flat two-dimensional (2D) monolayer carbon,^{27–29} is an ideal matrix to support the electrode materials due to its unique properties of high electronic conductivity ($16\,000\text{ S m}^{-1}$),³⁰ high specific surface area ($2630\text{ m}^2\text{ g}^{-1}$, theoretical value)³¹ and high mechanical strength ($\sim 1100\text{ GPa}$).³² The graphene contributes remarkably to improving the electrochemical performance of these metal oxides or sulfides, for it acts both as a buffer to mitigate the volume changes during conversion reactions and as a separator to prevent the particles from aggregating upon long-term cycling. In addition, it offers a conductive scaffold to maintain the reliable electric contact for active materials and also the electric contact between the active materials and current collectors, resulting in stable cycling performance and a high Li-storage capacity.³³

Yet to our best knowledge, no report is available on the synthesis and electrochemical properties of $\text{NiS}/\text{graphene}$ (NiS/G) hybrid. Herein, we report the synthesis of NiS/G hybrid by a facile one-pot hydrothermal method and investigate the effect of graphene on the crystallization habit and electrochemical properties of NiS . We found that NiS exhibits sheet-like structure in the presence of graphene, forming a unique sheet-on-sheet hybrid nanostructure, while it tends to form rod-like structures if graphene is absent. The introduction of graphene also brings obviously improved cycling stability and rate capability for NiS . The mechanisms for the formation of

State Key Laboratory of Silicon Materials, Key Laboratory of Advanced Materials and Applications for Batteries of Zhejiang Province, and Department of Materials Science and Engineering, Zhejiang University, Hangzhou, 310027, P. R. China.
E-mail: xiejian1977@zju.edu.cn; zhaoxb@zju.edu.cn; Fax: +86-571-87951451;
Tel: +86-571-87951451

† Electronic supplementary information (ESI) available: TG plot of NiS/G , XRD, HRTEM and SAED of bare graphene, low-magnification SEM image and EDS mapping of NiS/G , low- and high-magnification SEM images of bare NiS , TEM image of bare graphene, SAED of bare graphene and TEM image of NiS nanorod after electron beam irradiation, and specific capacity of NiS/G based on graphene or NiS . See DOI: 10.1039/c2ra22410k

NiS/G hybrid and the improvement in the electrochemical performance are proposed.

2. Experimental

2.1 Material preparation

For the preparation of ultrathin β -NiS nanosheet anchored on graphene, graphite oxide (GO, 40 mg), prepared by a modified Hummer's method,³⁴ was dispersed in 50 mL of deionized (DI) water with vigorous ultrasonic agitation for 3 h. Then, 1 mmol of $\text{NiCl}_2 \cdot 4\text{H}_2\text{O}$, 1 mmol of $\text{Na}_3\text{C}_6\text{H}_5\text{O}_7 \cdot 2\text{H}_2\text{O}$ and 3 mmol of thiourea were added to the above dispersion under stirring, followed by dropwise addition of 2 mL of ammonia solution (28 wt%) to tune the pH to 12. After being stirred for another 1 h, the mixture was transferred to a Teflon-lined stainless steel autoclave and heated in an electric oven at 180 °C for 24 h. Finally, the autoclave was allowed to cool down to room temperature naturally. The resulting black precipitate was collected by centrifugation, washed several times with DI water and absolute ethanol, and dried at 50 °C in vacuum overnight. Bare β -NiS and bare graphene were also prepared under the same conditions.

2.2 Material characterization

The morphology of the products was examined by using a field-emission scanning electron microscopy (FE-SEM, FEI-sirion), transmission electron microscopy (TEM, JEM 2100F) and high-resolution TEM (HRTEM, JEM 2100F) at 200 kV acceleration voltage. Crystalline phases of the products were identified using X-ray diffraction (XRD) on a Rigaku D/Max-2550pc powder diffractometer equipped with $\text{Cu-K}\alpha$ radiation ($\lambda = 1.54 \text{ \AA}$). Raman spectra were obtained with a Jobin-Yvon Labor Raman HR-800 Raman system by exciting a 514.5 nm Ar-ion laser. Thermogravimetry (TG) analysis was carried out in the temperature range of 25 to 700 °C at a heating rate of 10 °C min^{-1} in air. X-Ray photoelectron spectroscopy (XPS) measurements were performed on a KRATOS AXIS ULTRA-DLD spectrometer with a monochromatic Al $\text{K}\alpha$ radiation ($h\nu = 1486.6 \text{ eV}$).

2.3 Electrochemical measurements

The electrochemical measurements were carried out on the CR2025 coin-type cells. 75 wt% active material (NiS/G or bare NiS), 15 wt% acetylene black (Super-P), and 10 wt% polyvinylidene fluoride (PVDF) binder were mixed in *N*-methyl-2-pyrrolidinone (NMP) with magnetic stirring for 2 h. The electrode slurry was then coated onto Ni foam disks to form the working electrodes and dried at 110 °C under vacuum for 8 h. The electrodes were then assembled into half cells in an Ar-filled glove box with Li foil as the counter electrode, polypropylene microporous membrane (Celgard 2300) as the separator, and 1 M LiPF_6 dissolved in a mixture of ethylene carbonate (EC) and dimethyl carbonate (DMC) (1 : 1 by volume) as the electrolyte. Galvanostatic charge-discharge tests were performed on a NEWARE BTS-5V10mA battery cycler (Shenzhen, China) at various current densities between 0.05–3.0 V (vs. Li/Li^+). Cyclic voltammetry (CV) experiments were

conducted on an Arbin BT2000 system between 0.05 and 3.0 V (vs. Li/Li^+) at 0.1 mV s^{-1} . Electrochemical impedance spectroscopy (EIS) measurements were carried out on a CHI660C electrochemistry workstation in the frequency range from 100 kHz to 10 mHz at de-lithiation state. All of the electrochemical measurements were conducted at 25 °C.

3. Results and discussion

Fig. 1a shows the XRD patterns of the NiS/G hybrid and bare NiS. The XRD results reveal the formation of β -NiS (space group $R3m$, JCPDS No.03-0760) for both samples. No impurity phase is detected. For NiS/G, the broad hump at around $2\theta = 25^\circ$ is assigned to the restacked graphene sheets after the reduction of GO. The content of graphene is estimated to be 31.8 wt% according to the TG analysis (see ESI, Fig. S1†). The detailed explanation of the TG curve is given in the ESI (see ESI, Fig. S1†). Bare graphene, prepared by a similar route, was also characterized by XRD and selected area electron diffraction (SAED) to check its crystalline nature as shown in Fig. S2.† The results confirm the short-range order in stacked graphene sheets.^{35,36} The reduction of the GO was confirmed by Raman spectra as seen in Fig. 1b. Both GO and NiS/G exhibit two bands at 1350 and 1580 cm^{-1} , which are associated with the disordered (*D*) and graphitic (*G*) bands, respectively, of carbon-based materials.³⁷ Compared with GO, NiS/G shows an increased *D*-to-*G* intensity ratio, which is caused by the decrease of the average size of the sp^2 domains, while the quantity of these domains is increased.³⁸ The change in *D/G* intensity generally indicates the reduction of GO to graphene.³⁸

Fig. 1c gives XPS survey spectrum of the NiS/G, with the detected elements of Ni, S, C and O as expected for the hybrid. The two bands at about 855.3 and 873.0 eV, correspond to $\text{Ni}2\text{p}_{3/2}$ and $\text{Ni}2\text{p}_{1/2}$, respectively.³⁹ The band at 161.7 eV corresponds to $\text{S}2\text{p}_{3/2}$.³⁹ The presence of O peaks is due to the residual oxygen-containing groups in the reduced GO. C1s XPS measurements were performed to further check the reduction status of GO during the hydrothermal process. Fig. 1d compares the C1s spectra of the GO and NiS/G, where four peaks can be deconvoluted, corresponding to carbon atoms in different functional groups: sp^2 carbon ($\text{C}=\text{C}$, 284.8 eV), carbon in C–O bonds (286.2 eV), carbonyl carbon ($\text{C}=\text{O}$, 287.6 eV) and carboxylate carbon ($\text{O}=\text{C}=\text{O}$, 289.1 eV).^{38,40} Note that the peak intensity of the oxygenated carbon drops significantly after the hydrothermal reactions, indicating a sufficient reduction of GO.

SEM image of the NiS/G hybrid is shown in Fig. 2a. Note that the hybrid exhibits a sheet-like morphology. The energy dispersive X-ray spectroscopy (EDS) mapping in Fig. 2b indicates that carbon, oxygen, nickel and sulfur elements are present in the hybrid. Based on the EDS mapping, we can conclude that both graphene and NiS are in a sheet form. The O element comes from the residual oxygen-containing groups as mentioned above. Image of 300 times magnification is also supplied to present the overall morphology of the hybrid. The

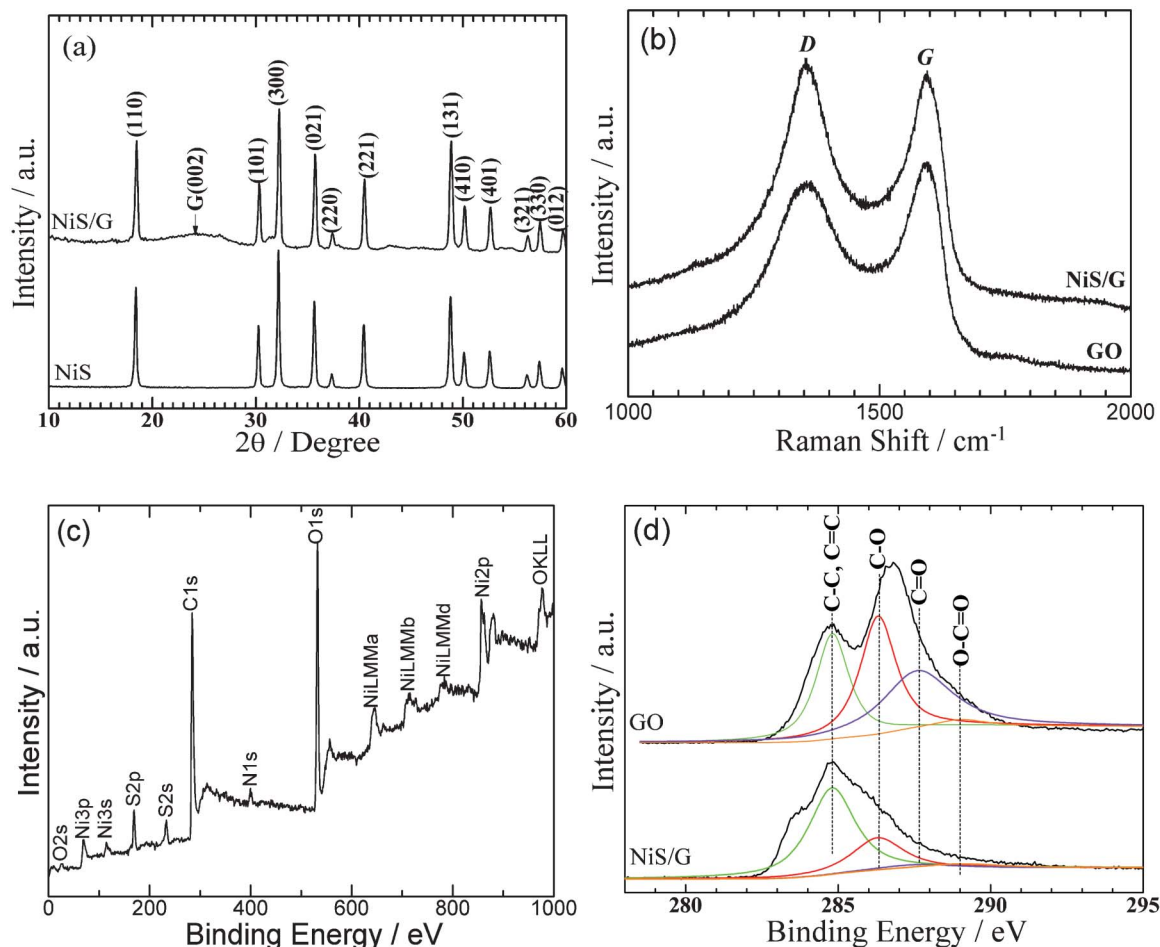


Fig. 1 (a) XRD patterns of NiS and NiS/G, (b) Raman spectra of GO and NiS/G, (c) XPS survey spectrum of NiS/G, and (d) C1s XPS of NiS/G and GO.

EDS mapping in the overall morphology was also given, which reveals that NiS is dispersed on graphene uniformly (see ESI, Fig. S3†). TEM and EDS analyses were carried out to check the microstructure and composition of the hybrid as shown in Fig. 3. The EDS analyses in three different regions in Fig. 3a

are given in Fig. 3b. The results clearly demonstrate that in all three regions, signals of carbon, nickel and sulfur are all present. In region a, the C peak shows a rather higher intensity compared with Ni or S peaks, indicating that the edge of the sheet-like structure is composed mainly of graphene. In region

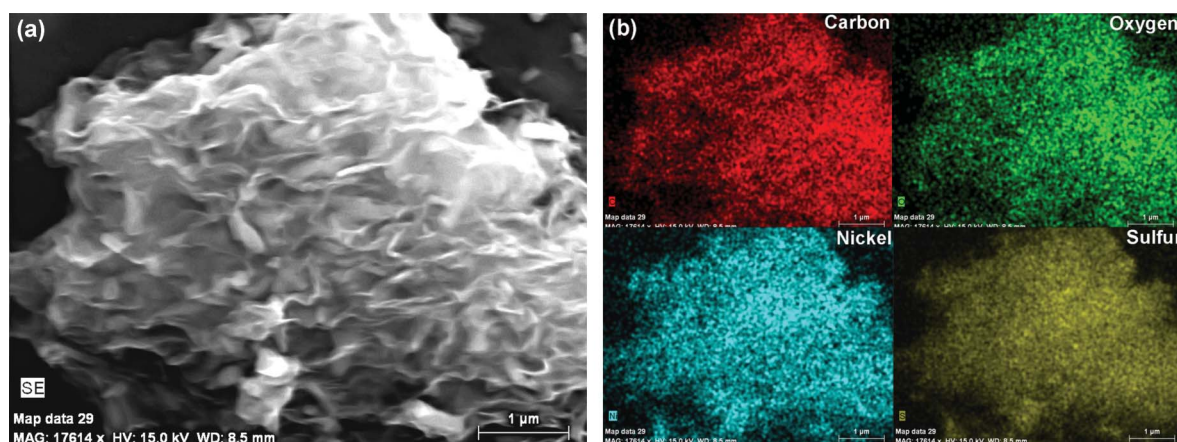


Fig. 2 (a) SEM image and (b) EDS mapping of NiS/G.

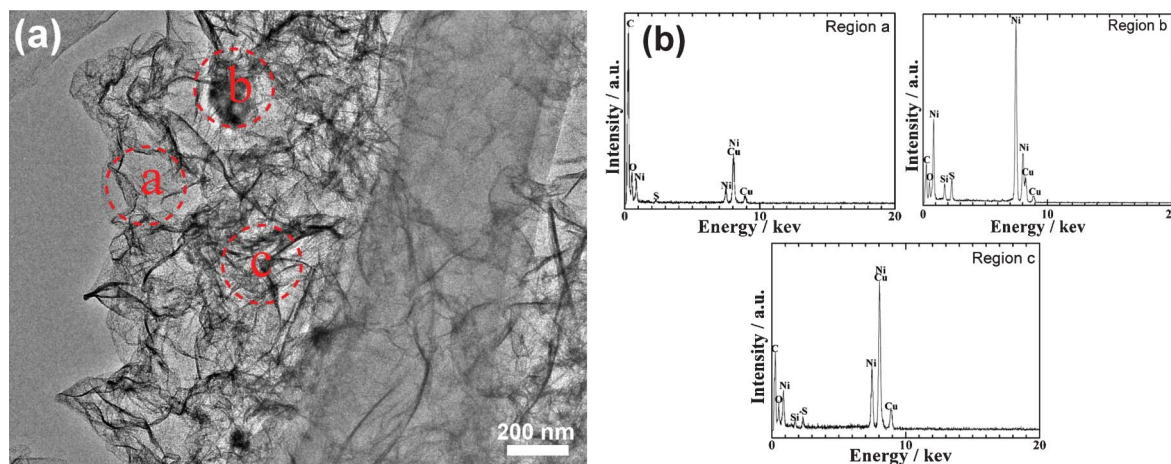


Fig. 3 (a) TEM image and (b) EDS of NiS/G.

b (the dark region), the higher C-to-S (or Ni) intensity ratio indicates that local aggregation of NiS occurs on graphene. Thus, a NiS/G hybrid with a sheet-on-sheet structure has formed by this one-pot hydrothermal route. The transparent nature of the hybrid suggests that both NiS and graphene are rather thin. For comparison, bare NiS was also prepared under the same conditions as those for NiS/G except that GO was not added in the precursors. Interestingly, bare NiS exhibits a rod-like structure (see ESI, Fig. S4†), while bare graphene exhibits a sheet structure (see ESI, Fig. S5†). It is obvious that graphene plays a critical role in changing the crystallization habit of NiS.

To further explore the microstructure of graphene and NiS nanosheets, HRTEM images of the NiS/G hybrid are characterized in the wrinkled area of the hybrid as indicated in Fig. 4. During the HRTEM characterization, we notice that there exists two kinds of lattice fringes. One is not well defined with an inter-layer distance (d -spacing) of around 0.38 nm, and the other is ordered with different d -spacings of 0.18, 0.22, and 0.25 nm (Fig. 4a). EDS analyses indicate that the ill-defined region is dominantly graphene with minor NiS, while the

ordered region is NiS loaded on graphene (Fig. 4b). Note that the graphene in the NiS/G hybrid is in few-layer form (below 8 layers) and is relatively stable upon electron beam irradiation for a short period of time even at 200 kV acceleration voltage, while the NiS sheets are unstable at this voltage and are rapidly decomposed from nanosheets into smaller nanoplates (below 5 nm), from which it can be seen that the NiS sheets are rather thin (below 5 nm). The damage of NiS upon electron beam irradiation is more clearly seen in bare NiS nanorod (see ESI, Fig. S6†). It should be noted that the measured value (around 0.38 nm) of the d -spacing of graphene is higher than that of perfectly crystallized graphite (0.335 nm). The higher d -spacing value of graphene compared with graphite is attributed to the presence of oxygen-containing groups. The d -spacing value thus is largely dependent on the deoxygenation state of graphene.^{40,41}

Based on the above analyses, a possible formation mechanism of the sheet-on-sheet structure of NiS/G is proposed and schematically illustrated in Fig. 5. It suggests that three factors determine the formation of this unique

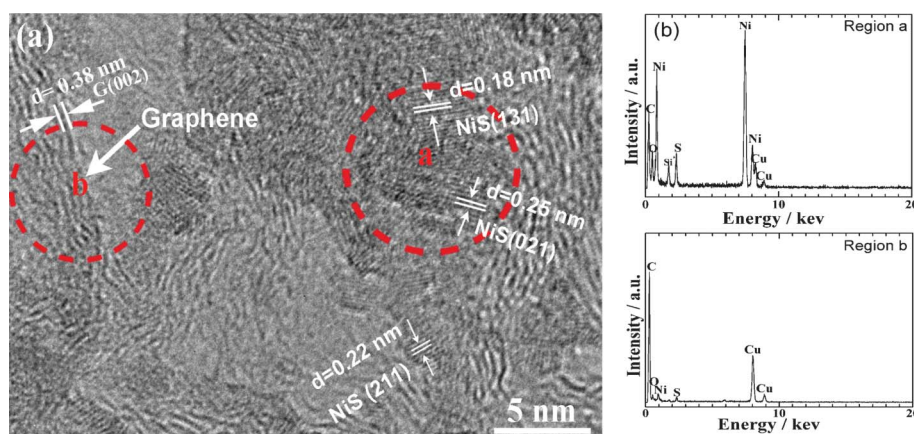


Fig. 4 (a) HRTEM image and (b) EDS of NiS/G.

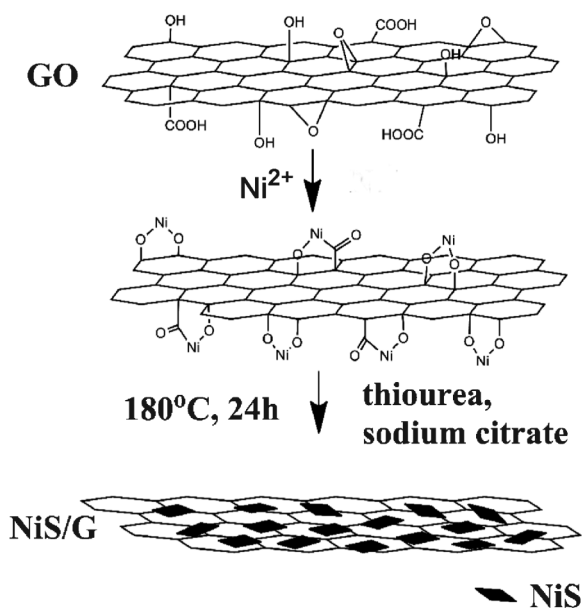


Fig. 5 Schematic illustration of the formation mechanism of NiS/G.

nanoarchitecture: (i) GO is sufficiently exfoliated into graphene oxide sheets in water by vigorous ultrasonic treatment; (ii) Ni^{2+} ions are uniformly dispersed onto the graphene oxide sheets by electrostatic force due to the negatively charged nature of graphene oxide in aqueous solution;⁴² (iii) The crystal growth of NiS can be confined in a 2D direction because of the confining effect of graphene sheets. Otherwise, NiS tends to grow into a rod-like structure when graphene is not introduced.

A series of electrochemical measurements on NiS/G and bare NiS were carried out to evaluate the effect of graphene on the electrochemical properties of NiS. Fig. 6a illustrates the first three charge–discharge curves with a cutoff voltage of 0.05–3 V at the current density of 50 mA g^{-1} . The specific capacities of NiS/G are calculated based on total mass of NiS and graphene. The first charge and discharge capacities of NiS/G are 723 and 1186 mAh g^{-1} , respectively, while those of bare NiS are 875 and 579 mAh g^{-1} , respectively. It can be seen that both samples show an irreversible capacity loss during the first cycle due to the formation of solid electrolyte interface (SEI) layer. Based on the theoretical capacity of NiS (590 mAh g^{-1}),⁹ the theoretical capacity of NiS/G is roughly estimated to be 500 mAh g^{-1} considering the content of graphene (31.8

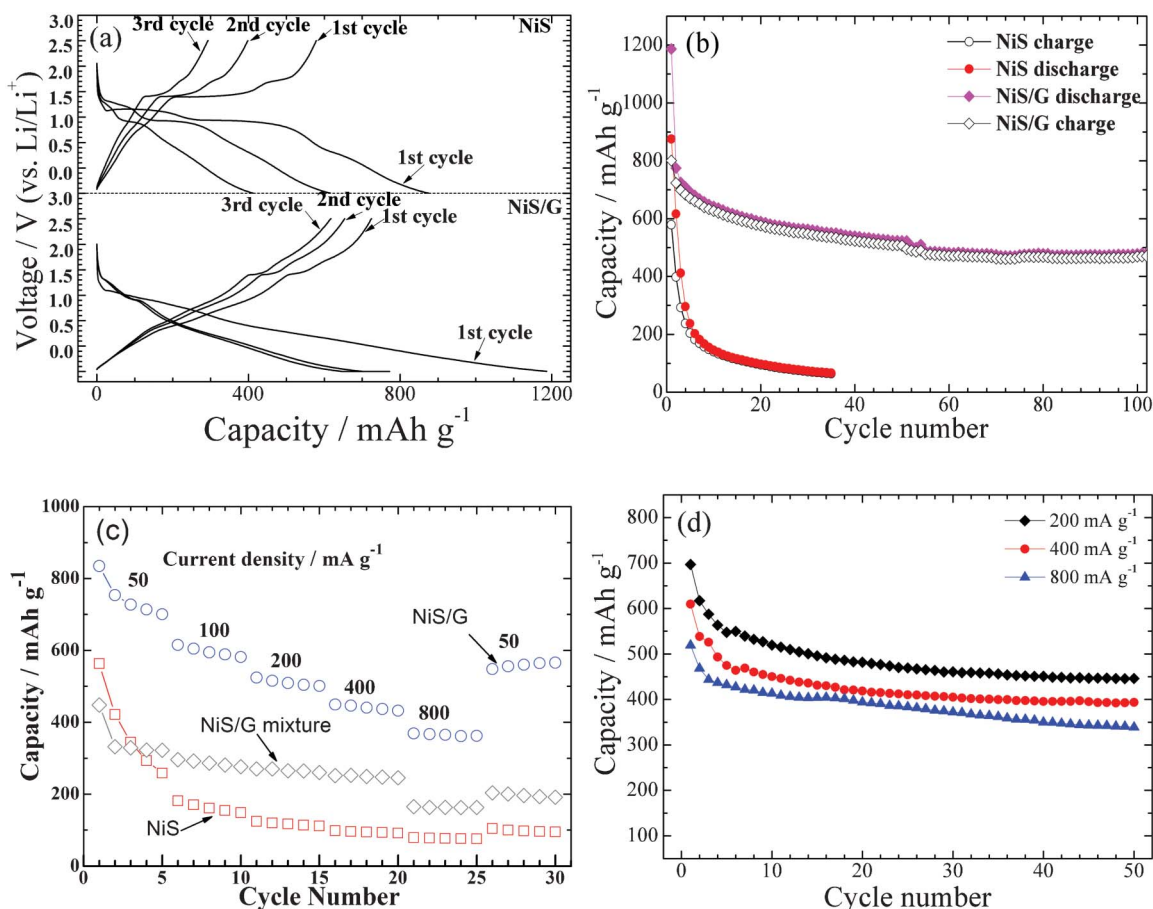


Fig. 6 (a) Voltage profiles and (b) cycling stability of NiS/G and NiS charged–discharged at 50 mA g^{-1} , (c) comparison of rate capability between NiS/G, NiS and NiS/G mixture charged at 50–800 mA g^{-1} and discharged at 50 mA g^{-1} , and (d) cycling stability of NiS/G charged at 200–800 mA g^{-1} and discharged at 50 mA g^{-1} .

wt%) and the obtainable capacity of bare graphene given in our previous report.⁴³ The specific capacities of NiS/G based on weight of bare NiS and bare graphene are higher than their respective theoretical or obtainable values (see ESI, Fig. S7†). This phenomenon can be attributed to the synergistic effect between NiS and graphene. First, the introduced NiS helps to exfoliate graphene sufficiently, which can bring additional capacity from the double-layer capacitance effect of graphene due to the increased contact area with the electrolyte;⁴⁴ second, the polymeric/gel SEI films formed during first discharge can generate pseudocapacitive effect similar to that observed in transition metal oxides;⁴⁵ third, the presence of graphene changes the crystallization habit of NiS from thick rods to thin sheets which is kinetically more favorable for Li storage.

Fig. 6b shows the cycling performance of NiS/G and bare NiS between 0.05 V and 3.0 V at 50 mA g⁻¹. It is evident that NiS/G electrode exhibits much better capacity retention than bare NiS. After 100 cycles, the NiS/G electrode still retains a charge capacity of 481 mAh g⁻¹, while bare NiS shows rapid capacity decay. The improved cycling stability can be attributed mainly to the buffering effect of graphene that effectively mitigates the large volume changes during the conversion reactions, as well as the immobilizing effect that prevents the aggregation of the NiS nanosheets.

Fig. 6c compares the rate capability between NiS/G and bare NiS. The electrodes are charged at various current densities (50–800 mA g⁻¹) and discharged at 50 mA g⁻¹. Obviously, the NiS/G electrode exhibits much better rate capability than the bare NiS electrode. At 800 mA g⁻¹ (1.5 C), NiS/G can yield a charge capacity of 386 mAh g⁻¹, higher than the theoretical capacity of graphite (372 mAh g⁻¹). By contrast, bare NiS cannot sustain cycling at high current densities. To further investigate the effect of graphene on the electrochemical performance of NiS, we prepared a NiS/G hybrid by mechanically mixing bare NiS nanorods and graphene nanosheets (NiS/G mixture). The graphene content in the NiS/G mixture is controlled to be the same as that in *in situ* prepared NiS/G. The result shows the rate capability of NiS/G mixture is better than bare NiS, but inferior compared with the *in situ* prepared sample, indicating that the introduction of graphene not only affects the morphology and particle size but also plays an important role in enhancing the electrochemical performance of NiS. The best rate capability of the *in situ* prepared NiS/G is considered to originate from three factors: (i) graphene nanosheets with superior electronic conductivity supply 2D conducting networks for NiS nanosheets; (ii) the ultrathin feature of NiS nanosheets is favorable for rapid Li-ion diffusion in bulk NiS; (iii) the unique sheet-on-sheet structure of the hybrid is beneficial for better wetting of the active material and the rapid Li-ion transport across the electrode/electrolyte interface.

The charge capacity vs. cycle number at large current densities is plotted in Fig. 6d. The NiS/G electrodes were charged at 200, 400 and 800 mA g⁻¹, while the discharge current was fixed at 50 mA g⁻¹. An initial charge capacity of

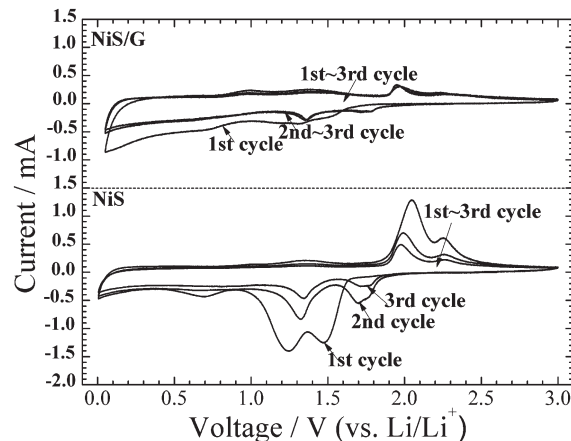
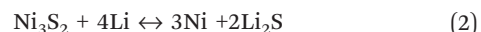
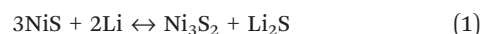


Fig. 7 CV plots of NiS/G and NiS scanned at 0.1 mV s⁻¹.

696 mAh g⁻¹ can be obtained at a current density of 200 mA g⁻¹ and the capacity can be kept at 446 mAh g⁻¹ after 50 cycles. At 400 mA g⁻¹, it can also retain a capacity of 394 mAh g⁻¹ after being cycled for 50 times. Even at 800 mA g⁻¹, the NiS/G electrode can still yield an initial charge capacity of 519 mAh g⁻¹ and maintain it at 339 mAh g⁻¹ after 50 cycles. Evidently, the introduction of graphene plays a critical role in improving the cycling stability of NiS at high current densities. Therefore, it is reasonable to expect that the NiS nanosheets can be attached firmly on the graphene nanosheets even after long-term cycling at high charge-discharge rates.

Fig. 7 shows CV plots of NiS/G and bare NiS, recorded at a scan rate of 0.1 mV s⁻¹ between 0.05 and 3.0 V. Cathodic peaks are present at around 1.5 and 1.2 V for the first cycle, and are shifted to 1.75 and 1.3 V in the second to third cycle, which might be associated with the two-step electrochemical reactions between NiS and lithium:⁹



The transformation from NiS to Ni₃S₂ is related to the cathodic peak at 1.75 V, while that from Ni₃S₂ to Ni is associated with the cathodic peak at 1.30 V. The anodic peaks at around 2.0 and 2.3 V correspond to the de-lithiation reactions and the recovery of NiS. Note that for NiS/G, the CV plots are almost overlapped after the first scan, indicating the reversible electrochemical reactions. In contrast, the peak intensity of bare NiS decreases with cycling due to the degradation of the electrode upon cycling.

To explain the different electrochemical behaviors between bare NiS and NiS/G, ac impedance plots were recorded after the cells have been cycled for 50 times as shown in Fig. 8. The Nyquist plots consist of a depressed semicircle in the high-to-middle frequency region and a sloping line in the low frequency region. The plots are fitted by an equivalent circuit given in the inset of Fig. 8. In the equivalent circuit, *R*_e denotes the electrolyte resistance, corresponding to the intercept of

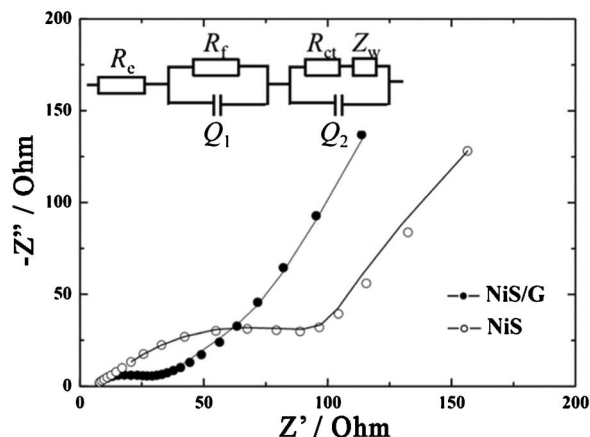


Fig. 8 Nyquist plots of NiS/G and NiS after charge-discharge at 50 mA g^{-1} for 50 cycles. The inset shows the equivalent circuit.

high-frequency semicircle at Z_{re} axis; R_f and Q_1 , which correspond to the high-frequency semicircle, denote the SEI layer resistance and dielectric relaxation capacitance, respectively; R_{ct} and Q_2 , corresponding to the middle-frequency semicircle, represent the charger transfer resistance and the related double-layer capacitance, respectively; Z_w is referred to the Warburg impedance, related to the Li-ions diffusion in the bulk electrode.⁴⁶ According to the fitting results, R_f and R_{ct} of bare NiS are 32.1 and 110.0 Ω , respectively, while those of NiS/G are 7.9 and 30.4 Ω , respectively. The better wetting of the NiS/G hybrid with a sheet-on-sheet structure and ultrathin sheet structure of NiS are responsible for its lower R_{ct} value. The higher R_f of NiS is caused possibly by the easier pulverization of micron (or sub-micron) rods and the continuous formation of new SEI layers. A lower R_{ct} of NiS/G can explain its better rate capability compared with bare NiS.

4. Conclusions

A hybrid based on NiS nanosheets and graphene nanosheets has been successfully synthesized by a facile one-pot route. The hybrid is constructed by ultrathin NiS sheets anchored on few-layer graphene sheets. The introduction of graphene changes the crystallization habit from nanorods to nanosheets due possibly to the electrostatic attraction between the precursors and the confining effect of graphene. The NiS/G hybrid exhibits obviously improved cycling stability and rate capability compared to bare NiS. The improved cycling stability is due mainly to the buffering effects of graphene, while the improved rate capability can be attributed to the 2D electronically conducting channels offered by graphene and the ultrathin feature of NiS, and the unique sheet-on-sheet structure of the hybrid. The good electrochemical properties of NiS/G make it a promising electrode material for secondary Li batteries.

Acknowledgements

We appreciate the support from the National Natural Science Foundation of China (No. 51101139), the Ph.D. Programs Foundation of the Ministry of Education of China (No. 20100101120024), the Foundation of Education Office of Zhejiang Province (No. Y201016484), the Qianjiang Talents Project of Science Technology Department of Zhejiang Province (2011R10021), and the Key Science and Technology Innovation Team of Zhejiang Province under grant number 2010R50013.

References

- 1 T. Takeuchi, H. Kageyama, K. Nakanishi, Y. Inada, M. Katayama, T. Ohta, H. Senoh, H. Sakaebe, T. Sakai, K. Tatsumi and H. Kobayashi, *J. Electrochem. Soc.*, 2012, **159**, A75–A84.
- 2 D. Zhang, X. L. Wang, Y. J. Mai, X. H. Xia, C. D. Gu and J. P. Tu, *J. Appl. Electrochem.*, 2012, **42**, 263–269.
- 3 D. Wang, M. Wu, Q. Wang, T. Wang and J. Chen, *Ionics*, 2010, **17**, 163–167.
- 4 Q. H. Wang, L. F. Jiao, H. M. Du, W. X. Peng, Y. Han, D. W. Song, Y. C. Si, Y. J. Wang and H. T. Yuan, *J. Mater. Chem.*, 2011, **21**, 327–329.
- 5 Q. H. Wang, L. F. Jiao, Y. Han, H. M. Du, W. X. Peng, Q. N. Huan, D. W. Song, Y. C. Si, Y. J. Wang and H. T. Yuan, *J. Phys. Chem. C*, 2011, **115**, 8300–8304.
- 6 Y. X. Zhou, H. B. Yao, Y. Wang, H. L. Liu, M. R. Gao, P. K. Shen and S. H. Yu, *Chem.-Eur. J.*, 2010, **16**, 12000–12007.
- 7 K. Zhang, W. Chen, L. Ma, H. Li, H. Li, F. Huang, Z. Xu, Q. Zhang and J. Y. Lee, *J. Mater. Chem.*, 2011, **21**, 6251–6257.
- 8 C. Zhang, Z. Wang, Z. Guo and X. W. Lou, *ACS Appl. Mater. Interfaces*, 2012, **4**, 3765–3768.
- 9 S. C. Han, K. W. Kim, H. J. Ahn, J. H. Ahn and J. Y. Lee, *J. Alloys Compd.*, 2003, **361**, 247–251.
- 10 N. H. Idris, M. M. Rahman, S. L. Chou, J. Z. Wang, D. Wexler and H. K. Liu, *Electrochim. Acta*, 2011, **58**, 456–462.
- 11 Y. Wang, Q. S. Zhu, L. Tao and X. W. Su, *J. Mater. Chem.*, 2011, **21**, 9248–9254.
- 12 S. C. Han, H. S. Kim, M. S. Song, P. S. Lee, J. Y. Lee and H. J. Ahn, *J. Alloys Compd.*, 2003, **349**, 290–296.
- 13 J. Wang, S. Y. Chew, D. Wexler, G. X. Wang, S. H. Ng, S. Zhong and H. K. Liu, *Electrochem. Commun.*, 2007, **9**, 1877–1880.
- 14 Y. Nishio, H. Kitauro, A. Hayashi and M. Tatsumisago, *J. Power Sources*, 2009, **189**, 629–632.
- 15 J. Z. Wang, S. L. Chou, S. Y. Chew, J. Z. Sun, M. Forsyth, D. R. MacFarlane and H. K. Liu, *Solid State Ionics*, 2008, **179**, 2379–2382.
- 16 S. B. Ni, X. L. Yang and T. Li, *J. Mater. Chem.*, 2012, **22**, 2395–2397.
- 17 W. Shi, J. Zhu, X. Rui, X. Cao, C. Chen, H. Zhang, H. H. Hng and Q. Yan, *ACS Appl. Mater. Interfaces*, 2012, **4**, 2999–3006.
- 18 J. Liu, W. Li and A. Manthiram, *Chem. Commun.*, 2010, **46**, 1437–1439.

- 19 M. Gu, Y. Li, X. L. Li, S. Y. Hu, X. W. Zhang, W. Xu, S. Thevuthasan, D. R. Baer, J. G. Zhang, J. Liu and C. M. Wang, *ACS Nano*, 2012, **6**, 8439–8447.
- 20 N. Liu, H. Wu, M. T. McDowell, Y. Yao, C. M. Wang and Y. Cui, *Nano Lett.*, 2012, **12**, 3315–3321.
- 21 Y. Huang, X. L. Huang, J. S. Lian, D. Xu, L. M. Wang and X. B. Zhang, *J. Mater. Chem.*, 2012, **22**, 2844–2847.
- 22 Y. Q. Zou and Y. Wang, *Nanoscale*, 2011, **3**, 2615–2620.
- 23 X. J. Zhu, J. Hu, H. L. Dai, L. Ding and L. Jiang, *Electrochim. Acta*, 2012, **64**, 23–28.
- 24 H. Hwang, H. Kim and J. Cho, *Nano Lett.*, 2011, **11**, 4826–4830.
- 25 K. Chang and W. X. Chen, *J. Mater. Chem.*, 2011, **21**, 17175–17184.
- 26 J. Xie, S. Y. Liu, G. S. Cao, T. J. Zhu and X. B. Zhao, *Nano Energy*, 2013, **2**, 49.
- 27 K. S. Novoselov, A. K. Geim, S. V. Morozov, D. Jiang, Y. Zhang, S. V. Dubonos, I. V. Grigorieva and A. A. Firsov, *Science*, 2004, **306**, 666–669.
- 28 K. S. Novoselov, A. K. Geim, S. V. Morozov, D. Jiang, M. I. Katsnelson, I. V. Grigorieva, S. V. Dubonos and A. A. Firsov, *Nature*, 2005, **438**, 197–200.
- 29 A. K. Geim and K. S. Novoselov, *Nat. Mater.*, 2007, **6**, 183–191.
- 30 C. H. Park, F. Giustino, C. D. Spataru, M. L. Cohen and S. G. Louie, *Nano Lett.*, 2009, **9**, 4234–4239.
- 31 M. D. Stoller, S. Park, Y. Zhu, J. An and R. S. Ruoff, *Nano Lett.*, 2008, **8**, 3498–3502.
- 32 C. Lee, X. Wei, J. W. Kysar and J. Hone, *Science*, 2008, **321**, 385–388.
- 33 J. Zhu, Y. K. Sharma, Z. Zeng, X. Zhang, M. Srinivasan, S. Mhaisalkar, H. Zhang, H. H. Hng and Q. Yan, *J. Phys. Chem. C*, 2011, **115**, 8400–8406.
- 34 W. S. Hummers and R. E. Offeman, *J. Am. Chem. Soc.*, 1958, **80**, 1339–1339.
- 35 Y. C. Si and E. T. Samulski, *Chem. Mater.*, 2008, **20**, 6792–6797.
- 36 J. S. Zhou, H. H. Song, L. L. Ma and X. H. Chen, *RSC Adv.*, 2011, **1**, 782–791.
- 37 F. Tuinstra and J. L. Koenig, *J. Chem. Phys.*, 1970, **53**, 1126–1130.
- 38 S. Stankovich, D. A. Dikin, R. D. Piner, K. A. Kohlhaas, A. Kleinhammes, Y. Jia, Y. Wu, S. T. Nguyen and R. S. Ruoff, *Carbon*, 2007, **45**, 1558–1565.
- 39 S. W. Goh, A. N. Buckley, R. N. Lamb, W. M. Skinner, A. Pring, H. Wang, L. J. Fan, L. Y. Jang, L. J. Lai and Y. W. Yang, *Phys. Chem. Miner.*, 2006, **33**, 98–105.
- 40 H. J. Shin, K. K. Kim, A. Benayad, S. M. Yoon, H. K. Park, I. S. Jung, M. H. Jin, H. K. Jeong, J. M. Kim, J. Y. Choi and Y. H. Lee, *Adv. Funct. Mater.*, 2009, **19**, 1987–1992.
- 41 H. Q. Chen, M. B. Mller, K. J. Gimore, G. G. Wallace and D. Li, *Adv. Mater.*, 2008, **20**, 3557–3561.
- 42 D. Li, M. B. Muller, S. Gilje, R. B. Kaner and G. G. Wallace, *Nat. Nanotechnol.*, 2008, **3**, 101–105.
- 43 S. Y. Liu, J. Xie, Y. X. Zheng, G. S. Cao, T. J. Zhu and X. B. Zhao, *Electrochim. Acta*, 2012, **66**, 271–278.
- 44 E. Yoo, J. Kim, E. Hosono, H. S. Zhou, T. Kudo and I. Honma, *Nano Lett.*, 2008, **8**, 2277–2282.
- 45 S. Laruelle, S. Grugeon, P. Poizot, M. Dolle, L. Dupont and J. M. Tarascon, *J. Electrochem. Soc.*, 2002, **149**, A627–A634.
- 46 D. Aurbach, *J. Power Sources*, 2000, **89**, 206–218.